Applied Catalysis B: Environmental 237 (2018) 772–782

Contents lists available at ScienceDirect

Applied Catalysis B: Environmental

journal homepage: www.elsevier.com/locate/apcatb

Hydrogenated heterojunction of boron nitride and titania enables the photocatalytic generation of H_2 in the absence of noble metal catalysts

Zuoli He, Chuhyung Kim, Tae Hwa Jeon, Wonyong Choi*

Division of Environmental Science and Engineering and Department of Chemical Engineering, Pohang University of Science and Technology (POSTECH), Pohang, 37673, South Korea

ARTICLE INFO

Keywords:
Photocatalysts
BN
TiO_2
H_2 generation
Heterojunction
Hydrogenated

ABSTRACT

The increasing need for new materials capable of solar fuel production is central to the development of green energy economy. Utilizing solar energy for hydrogen generation is a great challenge due to inefficient light utilization and fast charge recombination. In this work, disorder-engineered black H-TiO_2@BN with Ti-B chemically bonded interfaces was synthesized by employing BN nanosheets as the photocatalyst support. The hybridization of TiO_2 with BN and hydrogenated thermal treatment work synergistically to enable the photocatalytic H_2 production without noble metal cocatalysts. The hybrid photocatalyst markedly enhanced light absorption, significantly retarded charge pair recombination, facilitated interfacial electron transfer, and lowered interfacial charge transfer resistance. As a result, the photocatalytic H_2 production activity of H-TiO_2@BN that consisted of earth-abundant elements only was comparable to that of Pt-TiO_2. The present hybrid engineering for the efficient charge separation and transfer via the formation of the interfacial chemical bonds should provide a useful methodology for designing the new types of hybrid photocatalysts.

1. Introduction

Hydrogen is a clean energy resource that may replace fossil fuels in the future and the most ideal method of hydrogen production in a sustainable way is the solar photolysis of water. Semiconductor photocatalysis has emerged as a viable technology to achieve such goal to convert the solar energy to hydrogen energy [1–4]. Among a large variety of photocatalysts, titanium dioxide (TiO_2) based materials have many practical merits but it has a wide bandgap (about 3.2 eV, capturing less than 5% of solar energy) and its photoactivity is limited [5–9]. Various approaches have been employed such as scale-downing the particle size to nanometer, doping with metal or non-metal elements, constructing heterostructure, maximizing the exposure of specific facets, engineering interfacial properties, and hybridizing with other materials [9–15]. In particular, much effort has been devoted to making colored TiO_2 to enhance its optical absorption through doping or surface modification. As one of the most interesting works, "black titania" that was prepared via high pressure hydrogenated treatment was introduced as a visible light active photocatalyst [16,17]. A thin disordered amorphous TiO_2 hydrogenated layer encapsulating the anatase core of the nanoparticles induced a considerable narrowing of the optical band gap. The realization of black TiO_2 nanoparticles has opened a new strategy to enable the visible light absorption. The improved solar absorption is attributed to additional intermediate electronic states induced by the surface disorder [18–24]. There are many preparation methods for surface disordered black TiO_2 that reduces TiO_2 by hydrogen treatment in high pressure or high temperature, hydrogen plasma, chemical reduction (using Al, Zn, $NaBH_4$, CaH_2, etc.), and electrochemical reduction [22].

On the other hand, loading photocatalysts on new supports may provide a new route for preparing novel hybrid photocatalytic materials. BN is a good candidate support due to its low density, excellent chemical inertness and environment-friendly nature. Particular advantages of BN are the hydrophobic and layered structure [25–28]. There are several reports about the good performance of BN-based catalysts, including deep oxidation of volatile organic compounds, hydrogen production, oxygen reduction, water cleaning, and selective hydrogenation, etc [29–34]. The photocatalysts loaded on a layered structure facilitate the separation of electrons and holes and the subsequent charge transfer at the interface, which enhances the photocatalytic activity, while the hydrophobic support BN favorably adsorbs organic contaminants [33,35,36]. Likewise, layered or high surface area materials exhibit the high adsorption capacity for reactants resulting enhanced photocatalytic activity [30,37]. In hybrid photocatalysts, the presence of heterojunction interfaces provides charge discontinuity and built-in electric field which significantly affects

* Corresponding author.
E-mail address: wchoi@postech.edu (W. Choi).

https://doi.org/10.1016/j.apcatb.2018.06.008
Received 20 March 2018; Received in revised form 27 May 2018; Accepted 3 June 2018
Available online 04 June 2018
0926-3373/ © 2018 Elsevier B.V. All rights reserved.

charge transfer and following surface redox processes [14,38–42]. Therefore, interfacial structures between the photocatalytic material and the support should be precisely controlled to optimize the activities of hybrid photocatalysts.

Herein, we loaded TiO_2 on BN to design TiO_2@BN hybrid photocatalysts and investigated the photocatalytic H_2 production performance. The construction of hybrid photocatalysts is a valid strategy to facilitate the separation of electrons and holes at the interface between the two components. As for the hybrid photocatalysts, two most important problems should be resolved: I) engineering the interface for maximal charge separation; II) generating more charge carriers under light irradiation. In this work, the hydrogenated thermal treatment was employed to prepare disorder-engineered black hybrid photocatalysts (H-TiO_2@BN) which exhibited a highly enhanced activity of H_2 production. High temperature treatment induces the formation of chemically bonded interfacial structure which should facilitate the charge separation [43]. Hydrogenated treatment introduces more defect sites in the disordered surface and interface region that should enhance the visible light absorption and generate more charge carriers. So the interfacial chemical bond formation of Ti-B could also increase the visible light absorption and improve the charge transfer between TiO_2 and BN. The detailed characterizations, activity assessments, and mechanistic analysis of this new type of hybrid photocatalysts were investigated and discussed in this research.

2. Experimental section

2.1. Preparation of hydrogenated hybrid photocatalysts

All the chemical reagents were of analytical-grade purity (Sigma-Aldrich) and were used without further purification. The hydrogenated TiO_2@BN hybrid photocatalysts were synthesized by two steps. In the first step, boric acid (4 g) and urea (16 g) were mixed in 80 mL water at 80 °C for 4 h to form a clear colorless solution. After water was removed by a rotary evaporator, the mixed precursor solution was transferred into a quartz boat, which will transform into gels after cooling to room temperature. Then the quartz boat was put into a horizontal tube furnace, and then annealed to 900 °C for 5 h under N_2 gas. The white porous BN nanosheets were obtained after washing with water and ethanol. Because the BN sample could be well dispersed in the ethanol solution, and titanium isopropoxide could be used to grow TiO_2 nanoparticles on the surface of BN nanosheets. 0.40 g as-obtained BN nanosheets firstly dispersed in 80 mL ethanol. 2 mL titanium isopropoxide was added into the solution and kept at 60 °C for overnight, then most of the ethanol was removed using a rotary evaporator. The obtained sample was dried at 80 °C and named TiO_2@BN-80 °C, in which the mass percent of BN was 40%. In the second step, the black hydrogenated hybrid photocatalysts were obtained by annealing TiO_2@BN-80 °C at 700 °C in H_2 for 5 h and named as H-TiO_2@BN as shown in Figs. S1 and S2. For comparison, H-TiO_2, H-BN, various hybrid TiO_2@BN and H-TiO_2@BN samples were successfully prepared under different temperatures or atmospheres. TiO_2@BN-80 °C annealed at 700 °C in N_2 was named as TiO_2@BN.

2.2. Characterizations

X-ray diffraction (XRD; Rigaku, RINT 2000) was carried out to investigate the crystalline phase of different samples. The morphology and crystallography of the samples were examined using a field-emission scanning electron microscope (FE-SEM; JSM-7401 F and FEI QUANTA F250) and a high-resolution transmission electron microscope (HR-TEM; JEOL, JEM-2200FS) with the electron energy-loss spectroscopy (EELS) analysis, which was carried out at the National Institute for Nanomaterials Technology (NINT) in Pohang, Korea. X-ray photoelectron spectroscopy (XPS) and ultra-violet photoelectron spectroscopy (UPS) spectra were collected at Korea Basic Science Institute (KBSI) to investigate the surface chemical properties of the samples by AXIS-NOVA (Kratos. Inc) using a monochromatic Al Kα line (1486.6 eV) source for XPS, He (21.21 eV) UV source for UPS, respectively. The shift in the binding energy due to the relative surface charging was corrected according to the C 1s level at 284.6 eV as an internal standard. UV–vis absorption spectra were recorded on a UV–vis spectrophotometer (Shimadzu UV-2600). Fourier transform infrared spectroscopy (FT-IR) was recorded with pelletized samples on a Thermo Scientific Nicolet iS50 FT-IR spectrophotometer, equipped with an iS50 ATR accessory (Thermo Scientific, Madison, USA).

2.3. Photocatalytic H_2 production measurements

The photocatalytic activities of the as-synthesized samples were measured in an aqueous suspension in a pyrex reactor for H_2 production, where 10 vol% methanol was added as an electron donor. For the H_2 production experiments, 15 mg photocatalyst was dispersed in 27 mL distilled water under sonication for 3 min in an ultrasonic cleaning bath. The pH of the suspension was adjusted to 3.0 with concentrated $HClO_4$ after adding 3 mL methanol. Then the aqueous methanol solution was transferred into the pyrex reactor, which was sealed with a rubber septum. The reactor was purged with Ar gas for 30 min prior to irradiation to remove dissolved oxygen. A 300-W Xe-arc lamp (Oriel) was used as the light source for the photocatalytic reactions. Light was passed through a 10-cm IR water filter and a cutoff filter ($\lambda > 320$ nm), and then the filtered light was focused onto a 55.5 mL pyrex reactor. The photo-produced H_2 was analyzed in the headspace of the sealed reactor by using a gas chromatograph (GC, HP6890 A) with a thermal conductivity detector and Ar as a carrier gas. The stability of photocatalytic H_2 production activity was measured by repeating the photocatalysis cycles in the same sealed pyrex reactor containing the same batch of catalyst, the catalyst suspension was purged with Ar gas for 30 min at the end of each irradiation cycle.

The apparent quantum yields (AQY) for H_2 production defined by Eq. (1) were measured by using monochromatic irradiation filtered by Newport Oriel 77250 Monochromator and measured by a NOVA power monitor). The AQY was calculated as follow:

$$\text{A. Q. Y. } [\%] = \frac{number\ of\ evolved\ H_2\ molecules \times 2}{number\ of\ incident\ photons} \times 100 \quad (1)$$

2.4. Photoelectrochemical measurements

Two types of photoelectrochemical (PEC) measurements (electrode or slurry test) were carried out in a conventional three-electrode system connected to a potentiostat (Gamry, Reference 600). The slurry photocurrent collection tests were also conducted in a suspension of catalysts with a Pt wire, a graphite rod, and an Ag/AgCl electrode as a working, counter, and reference electrode, respectively, under continuous stirring and Ar gas purging. The electrons generated on photocatalysts in suspension were collected on a working electrode (Pt, biased of +0.6 V (vs. Ag/AgCl)) through electron shuttles (using a reversible redox couple of Fe^{3+}/Fe^{2+}) under light irradiation. The same 300-W Xe-arc lamp (Oriel) used in the photocatalysis experiments was also employed as the light source.

PEC measurements were performed in a typical three-electrode potentiostat system, in which the photocatalyst film on a FTO substrate, a Pt wire, and an Ag/AgCl electrode were used as a working, counter, and reference electrode, respectively. These three electrodes were immersed in an aqueous electrolyte solution (0.2 M $NaClO_4$ at pH 3.0), and continuously purged Ar gas during the measurement. The photoelectrodes were prepared using a doctor blade method. Viscous photocatalyst paste was prepared by mixing the as-obtained catalyst powder, ethanol, terpineol, and ethyl cellulose (the weight ratio is about 2:10:4:1) under continuous grinding in an agate mortar for about 5 h. The paste was coated on an FTO glass by a doctor blade technique and then dried at 80 °C for 4 h. Finally, the as-obtained photoanodes

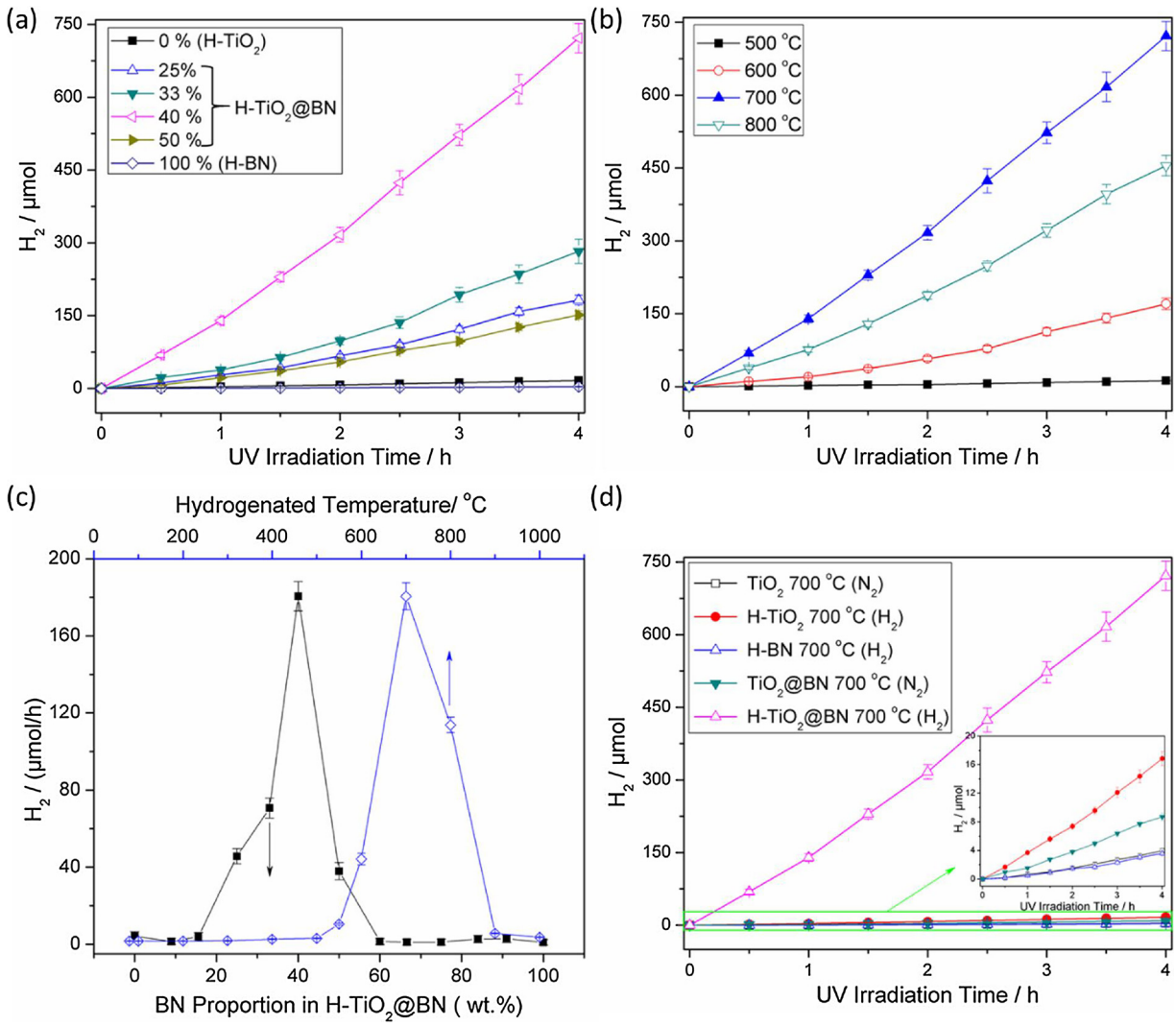

Fig. 1. Time profiles of photocatalytic production of H_2 in the presence of various H-TiO_2@BN samples: (a) H-TiO_2@BN with different BN proportion annealed at 700 °C in H_2 for 5 h. (b) H-TiO_2@BN with 40 wt% BN annealed in H_2 at different temperatures for 5 h. (c) The H_2 production activity as a function of the BN proportion and the annealing temperature. (d) The comparison of the photocatalytic H_2 production activities with the control samples (TiO_2, BN, and TiO_2@BN (with 40 wt% BN)) annealed in H_2 or N_2 at 700 °C. Experimental conditions: 300-W Xe lamp (λ > 320 nm); [catalyst] = 0.5 g/L; [Methanol] = 10 vol%; pH = 3.0; initially Ar-saturated; a Pyrex glass reactor.

were sintered at 450 °C for 30 min in different atmospheres. The obtained photoelectrodes have an average active area of about 2 cm^2. Linear sweep voltammogram (LSV) and electrochemical impedance spectroscopy (EIS) were measured at applied bias from −1.0 to +0.5 V, and −0.3743 V (vs. Ag/AgCl), respectively. The open-circuit potential (OCP) and Mott–Schottky plots were also measured in $NaClO_4$ (0.2 M) electrolyte at pH 3.0. The open-circuit stationary potential in the dark (E_0) and under light irradiation (E_{ph}) was measured after equilibration. To ensure the reproducibility of the electrode behavior, the same electrode was used in the PEC measurements. The same 300-W Xe-arc lamp (Oriel) was also used in the PEC measurement as the light source as in the photocatalysis experiments. The Mott–Schottky plots were obtained by sweeping in positive direction at a frequency of 1000 Hz, the potential range from -1.0 to +1.0 V and the potential step 20 mV.

3. Results and discussions

3.1. Photocatalytic H_2 production activities of various TiO_2@BN samples

The photocatalytic H_2 production activities of the various H-TiO_2@BN samples were evaluated in the presence of methanol as a sacrificial reagent under light irradiation. Figs. 1a and b shows the effect of the BN content and hydrogenated temperature in H-TiO_2@BN samples on the photocatalytic H_2 production in the absence of any noble metal cocatalyst. The H-TiO_2@BN with 40% BN annealed at 700 °C for 5 h showed the highest activity among these samples. As shown in Figs. 1c and S3, H_2 production activity was not affected at all by loading BN up to 15%, then markedly increased above 20% loading with reaching a maximum at 40%, but rapidly decreased with further increase of BN loading and became negligible at 60%. The BN-induced increase of the photocatalytic activities might be ascribed to the facilitated charge separation across the interface between BN layer and TiO_2. The activities of the H-TiO_2@BN samples containing over 60% BN were as low as that of H-TiO_2, which could be attributed to the fact that BN layer itself has negligible light absorption in the irradiation region of λ > 320 nm but blocks the reactive surface sites on TiO_2 with shielding the incident light irradiation. As for the temperature effect, the photocatalytic activity was negligibly low below 500 °C, sharply increased above 550 °C and reached a maximum at 700 °C. However, it rapidly decreased above 700 °C and then became negligible above 900 °C. As the control tests, we also measured and compared the photocatalytic H_2 production activities of bare TiO_2, H-TiO_2, H-BN, and TiO_2@BN that were annealed

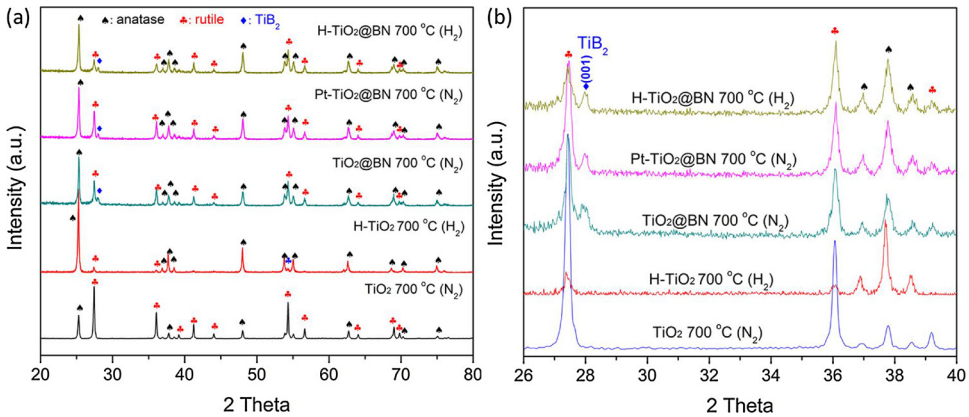

Fig. 2. XRD patterns of TiO_2, H-TiO_2 and various TiO_2@BN with 40 wt% BN samples.

in H_2 or N_2 at 700 °C (*see* Fig. 1d; other control samples' activities shown in Figs. S4-S6). The photocatalytic activities of H_2 production of bare TiO_2 and bare BN samples, regardless of whether they were hydrogenated or not, were negligibly small compared with the hydrogenated hybrid photocatalyst with 40 wt% BN (H-TiO_2@BN). The bare BN annealed in H_2 at 700 °C produced only 7 μmol H_2 and the bare TiO_2 annealed in H_2 at 700 °C generated only 18 μmol H_2 whereas the H-TiO_2@BN treated under the same condition produced over 700 μmol H_2 after 4 h light irradiation. Considering that both H-TiO_2 and H-BN exhibited insignificant photocatalytic activities for H_2 production (*see* Fig. 1d), the new interfacial layer formed between TiO_2 and BN should play an efficient catalytic role like Pt for H_2 production. The presence of heterojunction interface between BN and TiO_2 is essentially required for H_2 generating mechanism. The role of H_2 treatment is also essential because the photocatalytic activity of TiO_2@BN that was annealed in N_2 (*instead of H_2*) was much lower compared with H-TiO_2@BN.

3.2. Structural features and physical properties

The hybrid photocatalysts were characterized by various advanced analytic tools. Since the BN content was optimized at 40% (*see* Fig. 1c), all the hybrid photocatalysts characterized in this study contained 40 wt% BN. First, their crystal structures before and after calcination were characterized by XRD. As shown in Fig. S7, there is a clear diffraction peak around 26° in as-prepared TiO_2@BN-80 °C (air) sample, which is attributable to the (002) planes of the graphitic BN [44]. After calcination in N_2 or H_2, the anatase and rutile peaks appeared as shown in Fig. 2. However, the diffraction peak for BN was not clearly observed probably because the BN and anatase peaks overlap around 26°. It is noted that the hydrogenation treatment favored the formation of anatase phase. TiO_2 annealed in N_2 at 700 °C has 23% anatase and 77% rutile phases, whereas H-TiO_2 exhibited 95% anatase and 5% rutile. TiO_2@BN annealed in N_2 at 700 °C showed 72% anatase and 28% rutile phases but H-TiO_2@BN did 84% anatase and 16% rutile. In the enlarged XRD patterns shown in Fig. 2b, there are small peaks located at 27.54°, which is attributed to the (001) plane of the hexagonal TiB_2 [45,46]. It indicates that the Ti-B bonds were formed at the interface between TiO_2 and BN.

To study the chemical composition and valence state of the elements in H-TiO_2, H-BN, and various TiO_2@BN samples, XPS analysis was conducted. As shown in Fig. 3a, the shoulder peak at 190.7 eV in the B 1s spectra is assigned to sp^3 B-N bonds in BN nanosheets [47]. A new peak located at 188.25 eV in the annealed hybrid samples appeared after calcination, which is ascribed to the formation of a chemical bond (-Ti-B-N-) between titania and boron nitride [32,48]. The low energy peak at 187.95 eV also corresponds to boron incorporated into the TiO_2 lattice through occupying O sites to form -Ti-B- bond. Accordingly, the formation of the -Ti-B- bonds is also confirmed in the Ti 2p spectra.

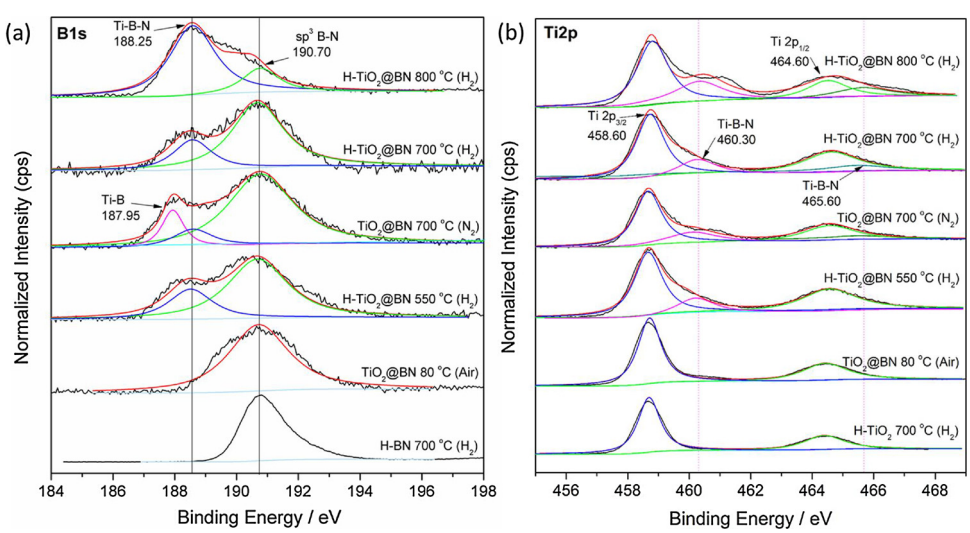

Fig. 3. Comparison of high-resolution XPS B 1s (a) and Ti 2p (b) spectra for H-BN, H-TiO_2 and various TiO_2@BN samples with 40 wt% BN.

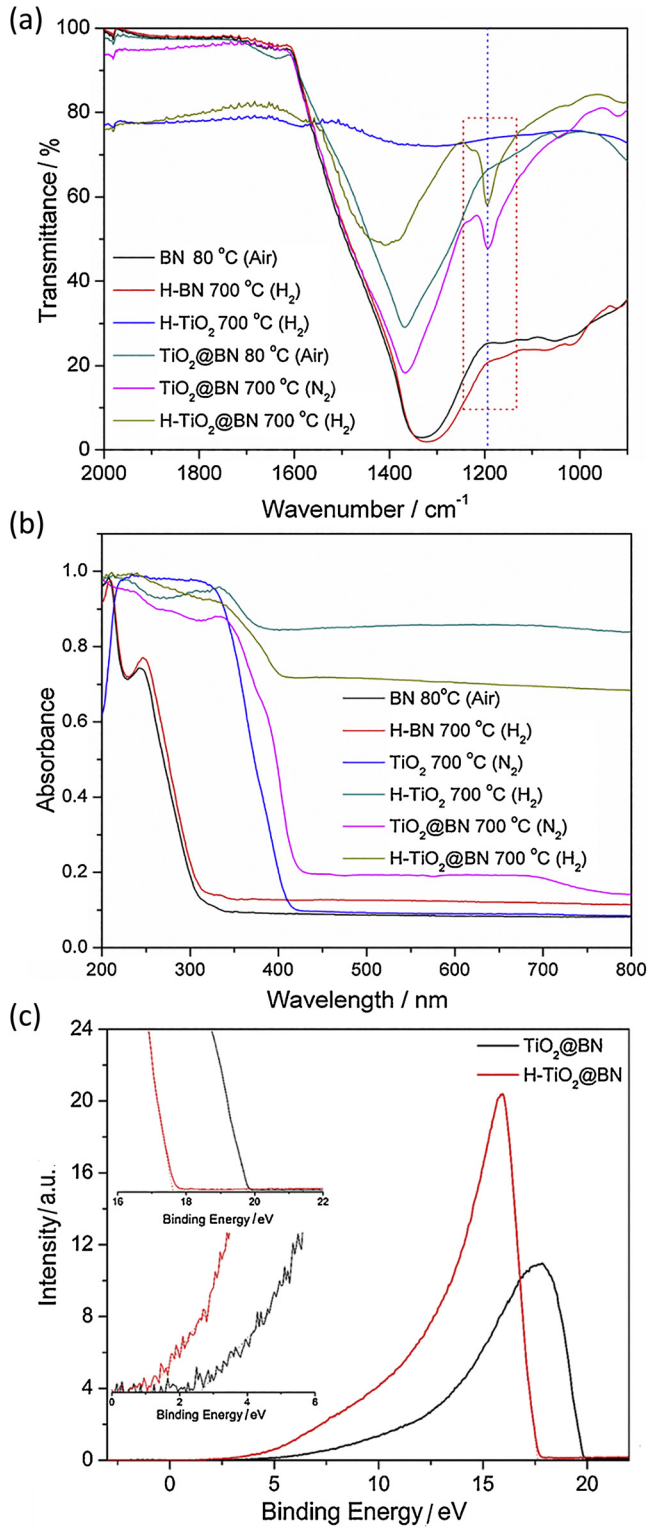

Fig. 4. Typical (a) FT-IR and (b) UV–vis absorption spectra of TiO_2, H-TiO_2, BN, BN and various TiO_2@BN samples with 40 wt% BN; (c) Ultraviolet photoelectron spectra (He I) for TiO_2@BN and H-TiO_2@BN films.

From Ti 2p spectrum of the annealed TiO_2@BN hybrid samples in Fig. 3b, it can be seen that two main peaks centered at 458.7 and 464.6 eV of Ti $2p_{3/2}$ and Ti $2p_{1/2}$, and two additional peaks located around 460.3 and 465.6 eV compared with TiO_2 and H-TiO_2, which is related with the hybridization with BN [43]. The O 1s peaks of TiO_2@BN samples (*see* Fig. S8), the two components are attributed to lattice oxygen (O_L) in TiO_2 (529.1 eV) and to surface OH (O_{OH}) species (531.4 ± 0.2 eV) as often reported for metal oxides [49]. By the way, the second peak located at 531.95 eV in TiO_2@BN sample showed a little shift to high energy due to the formation of N-O bonds. The FT-IR spectra of BN and H-BN samples in Fig. S9 showed intense absorption at 1375 and 787 cm^{-1}, which are ascribed to the characteristic stretching (ν_{B-N}) and bending modes (δ_{B-N}) of the hybridized BN skeletons, respectively [33,50]. Besides, the presence of a shoulder absorption peak at 1101 cm^{-1} (δ_{B-O}) indicates the existence of the bridge B-O-B in the BN network [50]. As shown in Fig. 4a, the FT-IR spectra of the TiO_2@BN samples annealed at 700 °C showed a new absorption peak around 1200 cm^{-1} corresponded to stretching modes of Ti-B, which also supports that Ti-B bond was formed in the annealed hybrid samples.

The visible light absorption characteristics of various TiO_2@BN samples were examined by diffuse reflectance spectroscopy (DRS). As shown in Fig. 4b, the annealed TiO_2@BN samples showed an elevated background in the region of 400–700 nm, which might be related to the presence of Ti-B bonds at the interface [45]. Furthermore, for hydrogenated samples, the band edge shifted to longer wavelengths. In particular, H-TiO_2 exhibited significantly enhanced absorption in the visible and near-infrared region compared with TiO_2@BN, H-TiO_2@BN. Such enhanced light absorption in hydrogenated samples is ascribed to disorder states induced by hydrogenated treatment with narrowing the bandgap [21,23]. It is noted that the intensity of this band is also related to the BN percentages and hydrogenated temperatures as shown in Figs. S3 and S10 in the supporting information. To investigate the valence band maximum (V_{VBM}) of TiO_2@BN and H-TiO_2@BN, their energy levels were determined by ultraviolet (UV) photoelectron spectroscopy (UPS) as shown in Fig. 4c. According to the spectra, V_{VBM} of the non-hydrogenated and hydrogenated hybrid photocatalyst film is located at *ca.* 2.46 and 1.19 eV (below the Fermi level), respectively. The difference of V_{VBM} might be ascribed to the surface defects of oxygen vacancies caused by hydrogenation [18,19].

To investigate the morphologies and microstructures of the samples, scanning electron microscopy (SEM), transmission electron microscopy (TEM) and high-resolution transmission electron microscopy (HR-TEM) examinations were carried out. Fig. S11 showed the typical SEM and TEM images of the BN sample and Fig. S12 showed the typical SEM images of H-TiO_2@BN samples (from now on, the hybrid photocatalysts with 40 wt% BN that were annealed at 700 °C in N_2 and H_2 is referred as TiO_2@BN and H-TiO_2@BN, respectively). The BN nanosheets showed a porous interconnected network and many pores were found on the surface. The HR-TEM images showed the porous nanosheets were composed of 3–5 stacked layers and were about 5 nm thick. During the synthesis process, the decomposition of boric acid and urea released gas like NH_3, N_2, and CO_2, which created bubbles and suppressed the h-BN growth in this region with forming the porous structure [37]. As shown in Fig. S12, the TiO_2 nanospheres with the diameter of ~200 nm were grown on the surface of BN. The microstructure of the H-TiO_2@BN was further investigated by HR-TEM (Figs. 5a–d), which shows that the hybrid samples were composed of TiO_2 nanoparticles and BN nanosheets. The interlayer distance of the planes at the edge is about 0.34 nm (Figs. 5c and d) corresponding to the (002) interplane distance of BN, while the interlayer distances corresponding to anatase and rutile phased TiO_2 were also found. It should be also noted that the (002) interplanes of BN were found on the surface, which implies the TiO_2 nanoparticles filled the pores. As a result, the pore structure which was clearly observed in bare BN was not found clearly in H-TiO_2@BN because the pores were filled with TiO_2. Element mapping of H-TiO_2@BN gave a uniform distribution of B, O, N and Ti element throughout the whole selected area.

One prominent feature of such hybrid structure as a catalytic reaction platform is the presence of active sites at the interfacial region. In particular, the reducing active sites play an important role in H_2 production. Monitoring the photocatalytic Pt deposition from the reduction reaction induced by the photogenerated electrons (for example, $Pt^{4+} + 4e^- \rightarrow Pt^0$) provides a straightforward method for observing the

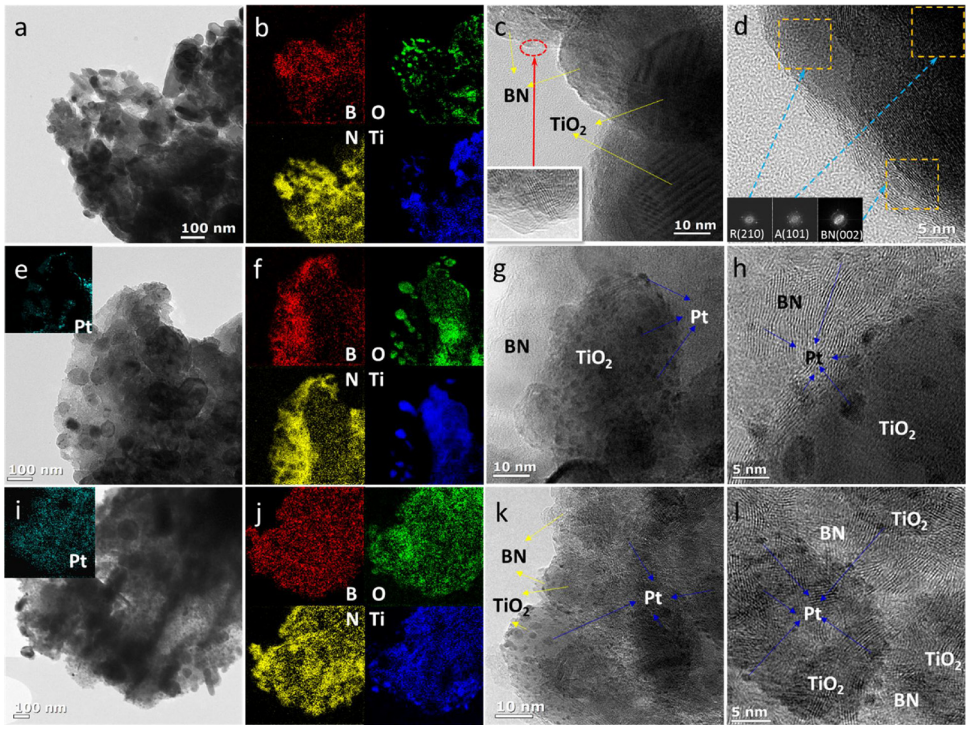

Fig. 5. HR-TEM images and EELS mapping data of H-TiO_2@BN (a–d), Pt-TiO_2@BN (e–h) and Pt-H-TiO_2@BN (i–l).

distribution of reducing active sites [51]. Figs. 5e–h showed the photodeposition of Pt particles on TiO_2@BN. The distinct feature observed in HR-TEM images (Figs. 5g and h) were that Pt particles were mainly deposited on the surface of the TiO_2 nanoparticles and interface of TiO_2 and BN. This fact clearly indicates that the TiO_2 surface and interfacial region in the hybrid photocatalysts are the H_2 production site. On the other hand, the photodeposition of Pt on H-TiO_2@BN were compared in Figs 5i–l. Unlike the case of TiO_2@BN, the Pt elements are uniformly distributed over Pt-H-TiO_2@BN throughout the whole selected area, which means H_2 production reactions occurred on the whole surface of the H-TiO_2@BN. This indicates that the hydrogenate treatment will induce the disorder states in H-TiO_2@BN surface, which contains many defects as reducing active sites for H_2 production.

3.3. Comparison of photocatalytic H_2 production with Pt-loaded samples

The photocatalytic H_2 production activity of H-TiO_2@BN was compared with various 1% Pt-deposited samples (which were annealed at 700 °C in H_2 or N_2), such as Pt-BN, Pt-TiO_2, Pt-H-TiO_2, Pt-TiO_2@BN. A commercial TiO_2 loaded with 1% Pt (Pt-P25), which is well known to exhibit high photocatalytic activity of H_2 production, was also tested as a control sample. As shown in Fig. 6a, the photocatalytic activity of H-TiO_2@BN is comparable to Pt-deposited samples. Pt-TiO_2@BN showed the best performance among all the samples under the light irradiation with the 320 nm long-pass filter and the photocatalytic activity decreased in the following order: Pt-TiO_2@BN > Pt-P25 > Pt-TiO_2 > **H-TiO_2@BN** > Pt-H-TiO_2 > Pt-BN) whereas **H-TiO_2@BN** showed the highest activity under the light irradiation with the 420 nm long-pass filter (*see* Fig. 6b, the activity order: **H-TiO_2@BN** > Pt-TiO_2@BN > Pt-H-TiO_2 > Pt-P25 > Pt-TiO_2 > Pt-BN). All the tested catalysts exhibited no activity for H_2 production in the dark control conditions. We also examined the wavelength-dependent apparent quantum yield (AQY) of H_2 production under monochromatic light [52,53] (*see* Figs. 6c and S13). The durability of the photocatalyst activity was tested by repeating the photocatalytic cycles of H_2 production up to four times (4 h for each cycle) in the same batch of the photocatalyst, which exhibited the reasonable stability (*see* Fig. 6d). The total production of H_2 for H-TiO_2@BN at the first cycle was 721 μmol, but reduced to 567 μmol after 4th cycle (about 21% decrease). Note that the photocatalytic H_2 production activity of H-TiO_2@BN is consistently higher than that of Pt-H-TiO_2 throughout the multiple cycles. Fig. S14 showed the XRD patterns of H-TiO_2@BN before and after the photocatalytic reactions, which indicated that such hybrid photocatalysts were stable for the repeated uses. The TEM images of H-TiO_2@BN after the photocatalytic reactions were also shown in Fig. S15, which showed the presence of TiO_2 nanoparticles on the surface of BN nanosheets and the interlayer distance corresponding to BN. The hybrid photocatalysts are stable enough as a result of the high temperature calcination.

3.4. Photo-response behaviors of the hybrid photocatalysts

The photo-respond behaviors of H-TiO_2@BN and other samples were investigated by two ways: the Fe^{3+}/Fe^{2+} redox couple-mediated photocurrent measurement in the photocatalyst slurry (Fig. 7a) and the photocurrent measurement with the electrodes (FTO glass) deposited with the photocatalyst film (Fig. 7b). In the slurry-type measurement, the photocurrent collected in the light-irradiated catalyst suspension was markedly enhanced when TiO_2 (or H-TiO_2) was hybridized with BN. This implies that the charge pair separation in TiO_2@BN is enhanced by the presence of BN. The additional hydrogenated treatment further increased the photocurrent (H-TiO_2@BN), which agrees with its enhanced photocatalytic activity. The combination of BN and hydrogenated treatment works synergistically to maximize the H_2 production in H-TiO_2@BN sample. The highest photocurrent generation obtained with Pt-TiO_2@BN is also consistent with its highest photocatalytic activity (*see* Fig. 6) [32]. Fig. 7b showed the time profiles of the photocurrent density during the repeated On-Off cycles of light irradiation for bare TiO_2, H-TiO_2, TiO_2@BN, H-TiO_2@BN and various Pt-deposited samples (annealed at 700 °C in H_2 or N_2) in the electrode-type measurement. Pt-TiO_2 exhibited the highest photocurrent among all the samples probably due to the high charge separation efficiency at the Pt/TiO_2 interface but Pt-H-TiO_2 showed much lower photocurrent than Pt-

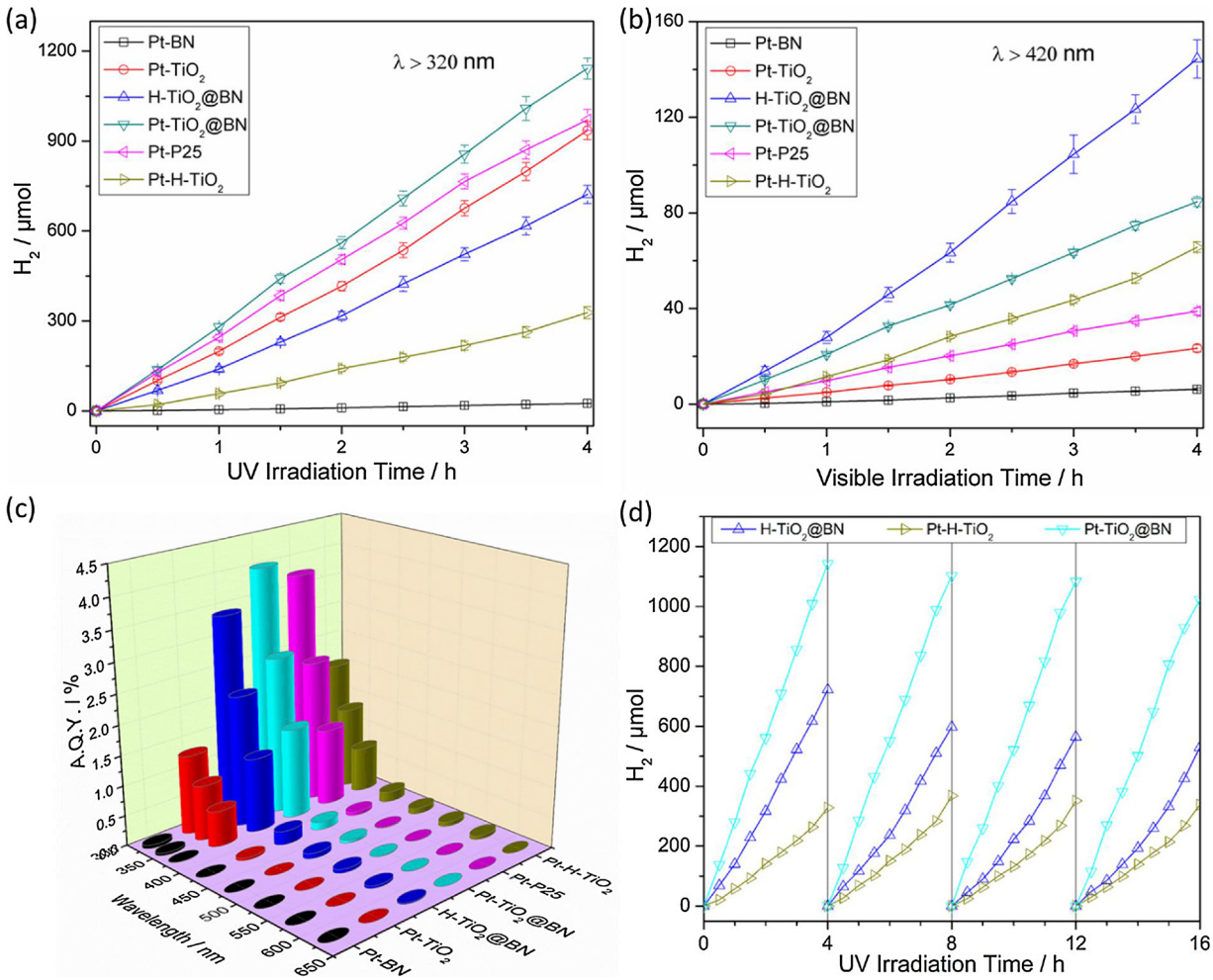

Fig. 6. Comparison of the photocatalytic performance of H-TiO_2@BN with various Pt-deposited samples for H_2 production under (a) UV light irradiation (λ > 320 nm) and (b) visible light (λ > 420 nm) irradiation; (c) Wavelength-dependent apparent quantum yield (AQY) of H_2 production over H-TiO_2@BN and various Pt-deposited samples; (d) Repeated cycles of H_2 production of H-TiO_2@BN compared with Pt-H-TiO_2 and Pt-TiO_2@BN under light irradiation (λ > 320 nm), the photocatalyst suspension was evacuated to remove the dissolved gases at the end of each cycle; (Experimental condition: 300-W Xe lamp as a light source, monochromatic light passed through a Newport Oriel 77250 Monochromator (for (b)); [catalyst] = 0.5 g/L; [Methanol] = 10 vol%; pH = 3.0; initially Ar-saturated; a Pyrex glass reactor with a window).

TiO_2, which might be related with the disordered surface states (induced by hydrogenated treatment) that may hinder the electron migration in the electrode. The photocurrent obtained from H-TiO_2 was significantly higher than that of pure TiO_2 because of its strong absorption of H-TiO_2 over the entire ultraviolet and visible light region. The hybridization of H-TiO_2 (or pure TiO_2) with BN or Pt reduced the photocurrent from that of bare ones although the loading of BN or Pt enhanced the photocatalytic activity of H_2 production on the contrary. However, this can be understandable considering the different measurement conditions between the photoelectrodes and suspended photocatalysts. The photogenerated electrons in a TiO_2-coated electrode should migrate through a series of particle boundaries to reach the FTO substrate to be collected as photocurrent [36]. Therefore, the defect and active sites should trap electrons as electron reservoirs during their migration through the particle grain boundaries, reducing the photocurrent reaching the FTO electrode [54,55]. The fact that the coupling of TiO_2 with BN similarly reduced the photocurrent implies that the TiO_2/BN interface holds electrons as the TiO_2/Pt interface does. This also supports the previous statement that the new interfacial layer formed between TiO_2 and BN should play an efficient catalytic role like Pt for H_2 production. In addition, it is interesting to note that the current time profile of H-TiO_2@BN is distinctively different from others. The slower rise and slower decay of photocurrent with H-TiO_2@BN implies that there seems to be charge-buffering sites. It is probable that the disordered surface or interface of H-TiO_2 and BN may serve as the charge buffering sites, which should enhance the photocatalytic H_2 production.

The normalized time profiles of open-circuit potential (OCP) decay (Fig. 7c) were also measured. The OCP decay upon turning off the light represents the charge recombination behavior in the electrode and showed the different recombination behaviors of trapped carriers in various electrodes [32,56]. Since the electron–hole pair recombination in TiO_2 lattice bulk is fast, the slow OCP decay observed for several minutes should be ascribed to the interfacial recombination between trapped charges and adsorbed species instead of the recombination in the lattice bulk. In comparison, OCP decay rate decreased in the order of TiO_2 > H-TiO_2 > TiO_2@BN > Pt-TiO_2 > Pt-H-TiO_2 > Pt-TiO_2@BN > H-TiO_2@BN, which is inversely correlated with the H_2 production activities. Pt-deposited samples have the higher photocatalytic activity of H_2 production because it exhibits the slower charge recombination. It should be noted that either BN hybridization or hydrogenated treatment alone retarded the OCP decay and the combination of both (H-TiO_2@BN) markedly retarded the OCP decay, which implies that BN hybridization and hydrogenated treatment induced the

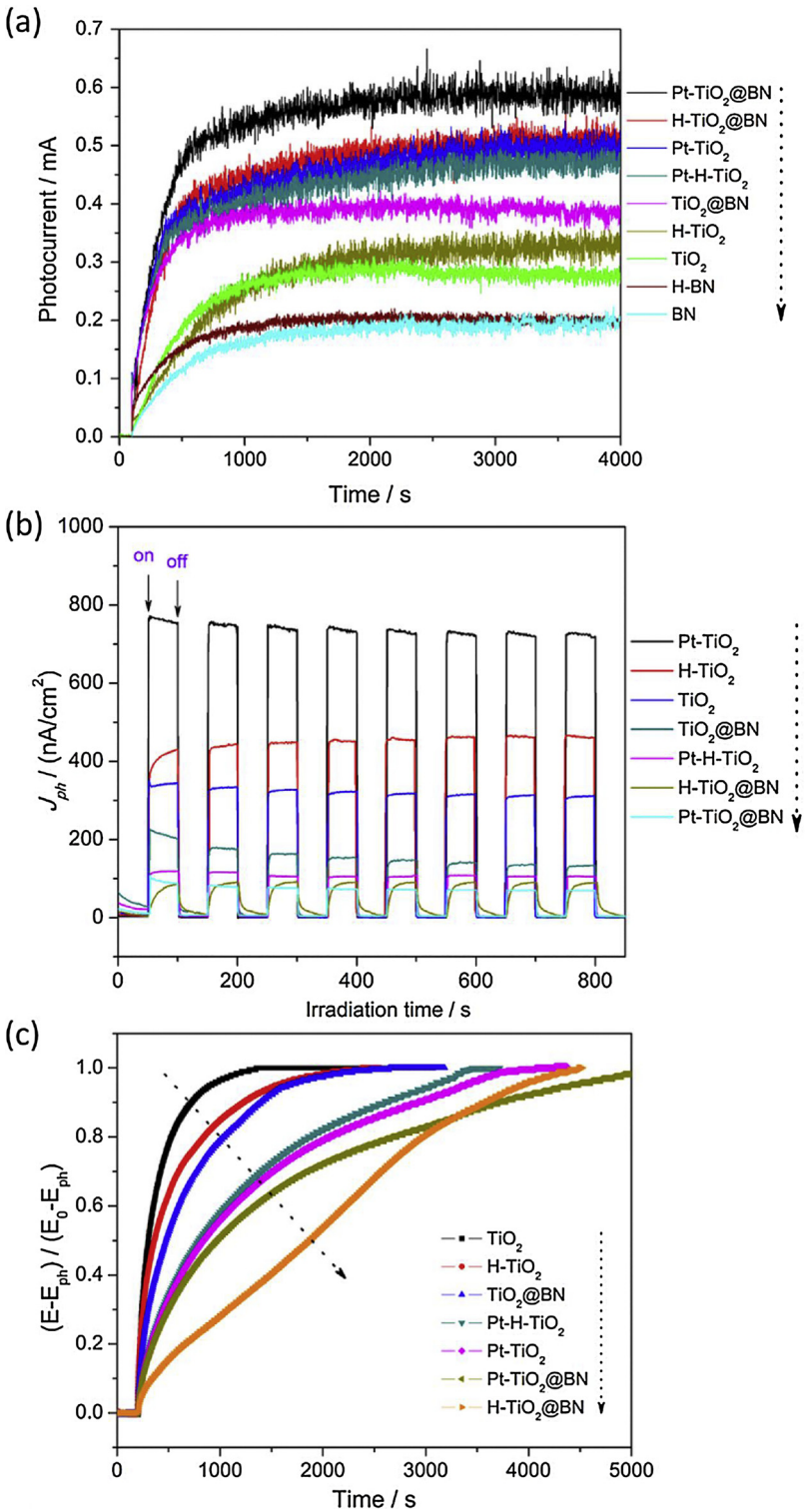

Fig. 7. (a) Time-dependent profiles of Fe^{3+}-mediated photocurrent in various photocatalysts suspensions under light irradiation. Experimental conditions: [catalyst] = 1 g/L; $[Fe^{3+}]$ = 0.5 mM; $[NaClO_4]$ = 0.1 M; pH = 1.8; Pt electrode held at +0.7 V (vs. Ag/AgCl); continuously Ar-purged; and λ > 320 nm; (b) Time profiles of photocurrent response under light irradiation (λ > 320 nm) with a potential bias of +0.6 V (vs. Ag/AgCl). (c) Normalized open-circuit potential (OCP) decay curves after turning off the light (E_0: steady-state potential in the dark, E_{ph}: steady-state potential under irradiation). Experimental conditions: $[NaClO_4]$ = 0.2 M; pH = 3.0; electrode area of 2 cm^2 and continuously Ar-purged; λ > 320 nm.

formation of charge-trapping defect sites. H-TiO_2@BN exhibits a much slower OCP decay rate than H-TiO_2 and TiO_2@BN, which is fully consistent with much higher photocatalytic activity of H-TiO_2@BN than that of H-TiO_2 and TiO_2@BN (*see* Fig. 6d). The distinctively different PEC behaviors of photocurrent generation and OCP decay in H-TiO_2@BN indicates that the heterojunction created between H-TiO_2 and BN plays a critical role in separating, trapping and transferring the charge carriers at the interfacial region for the subsequent H_2 production.

In the linear sweep voltammogram (LSV) of Fig. 8a, the onset potential for water reduction on H-TiO_2@BN electrode was slightly shifted to the positive direction compared with bare TiO_2 and TiO_2@BN. This is consistent with the observation that H-TiO_2@BN exhibited the enhanced photocatalytic production of H_2. The electrochemical impedance spectra (EIS) (Figs. 8b and S16) were also measured in the dark and under 320 nm irradiation. It is clear to see that the arc radii under irradiation are much smaller than those in the dark. Under irradiation, H-TiO_2@BN sample showed much smaller radii of the semicircular Nyquist plots compared to that of TiO_2@BN, which further confirms hydrogenated treatment could improve the interfacial charge transfer efficiency in hybrid photocatalysts. Pt-deposited samples also showed

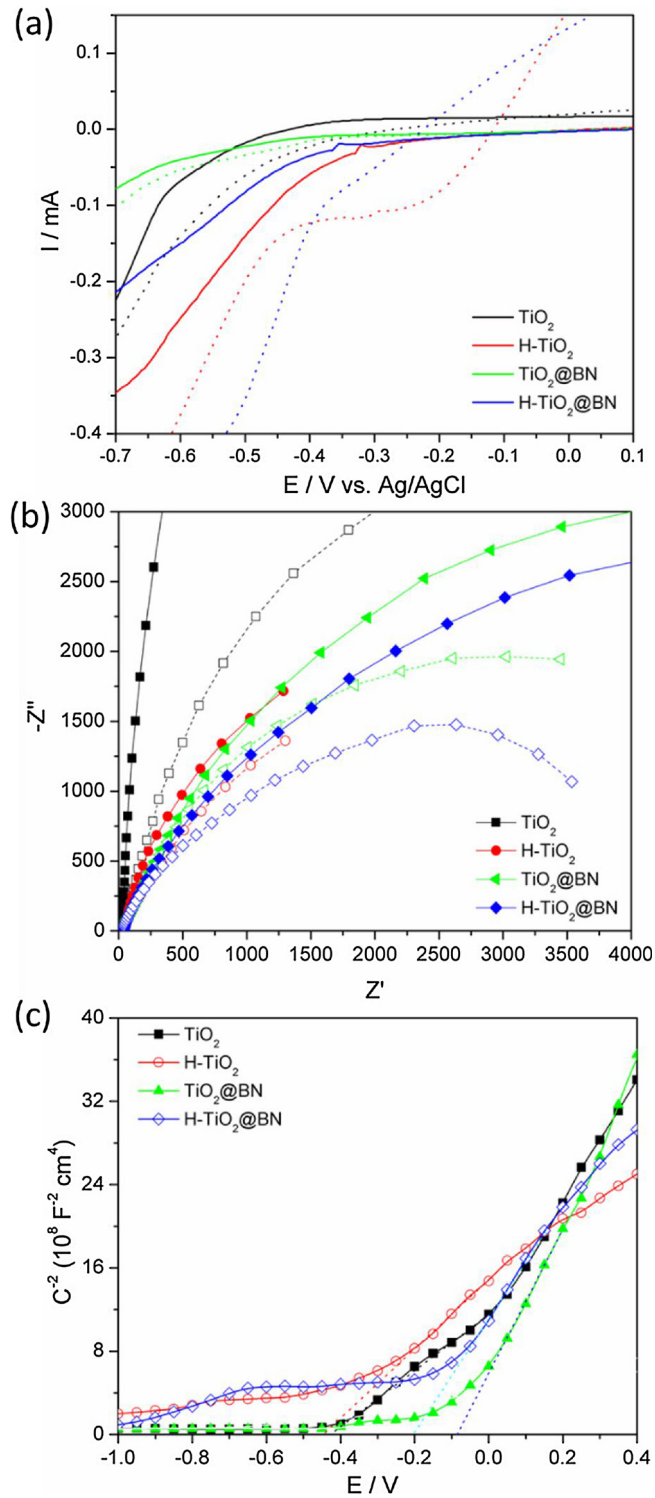

Fig. 8. (a) Linear sweep voltammograms (LSV) at scan rate 20 mV/s for the various electrodes in dark (solid line) and under light irradiation (dashed line); (b) Electrochemical impedance spectroscopy (EIS) Nyquist plots obtained in the frequency range of 0.01 Hz to 1000 Hz in the dark (solid line with filled symbol) and under light irradiation (dashed line with opened symbol); (c) Mott–Schottky plots collected at a frequency of 1000 Hz in the dark. Experimental conditions: [$NaClO_4$] = 0.2 M; pH = 3.0; electrode area of 2 cm^2; λ > 320 nm and continuously Ar-purged; applied bias for LSV and EIS were from -1.0 V to +0.5 V and -0.3743 V (vs. Ag/AgCl), respectively.

Table 1
Summary of photoelectron transport properties of various electrodes obtained from EIS modeling.

Samples	In dark			Under light irradiation		
	R_s / Ω	R_1 / Ω	C_1 / μF	R_s / Ω	R_1 / Ω	C_1 / μF
TiO_2	35.2	5794	1580	37.5	4108	1531
H-TiO_2	43.8	3049	3949	40.5	2581	4291
TiO_2@BN	42.9	4876	3439	43.2	3298	3484
H-TiO_2@BN	41.1	3700	660.9	41.5	2349	651.3
Pt-TiO_2@BN	48.8	574.7	183.7	48.9	327.9	176.1
Pt-H-TiO_2	49.2	882.8	131.7	49.1	482.5	128.4

R_s, electrode bulk resistance; R_1, charge transfer resistance; C_1, interfacial capacitance.

Table 2
The onset potential (E_{on}) obtained from LSV in dark and under UV light and flatband potential (E_{fb}) obtained from Mott–Schottky plots and for various electrodes at pH = 3.0.

Samples	V_{on} / V (Dark)	V_{on} / V (λ > 320 nm)	V_{fb} / V
TiO_2	−0.577	−0.496	−0.422
H-TiO_2	−0.373	−0.451	−0.446; −1.396
TiO_2@BN	−0.589	−0.587	−0.081; −0.481
H-TiO_2@BN	−0.412	−0.392	−0.204; −1.157
Pt-TiO_2@BN	−0.364	−0.343	−0.327
Pt-H-TiO_2	−0.361	−0.348	−0.556

more positive potentials of water reduction and more smaller arc radii than that of H-TiO_2@BN, indicating deposited Pt is an effective method to improve the photocatalytic H_2 production. The equivalent circuit R (CR) was used for fitting of the EIS plots data. Table 1 showed the values obtained from the equivalent circuit fitting. To further investigate the charge properties of the samples, a Mott-Schottky analysis was also carried out. Fig. 8c presents the Mott-Schottky plots of the samples; all the samples showed positive slopes in the Mott–Schottky plots, which indicate that they are n-type semiconductors [19,43]. H-TiO_2 and H-TiO_2@BN showed another slope at low potentials in the Mott–Schottky plots because of the hydrogenated treatment. Flatband potentials for H-TiO_2, TiO_2@BN, and H-TiO_2@BN clearly showed two different values as shown in Table 2, which means there are different types of donors in the samples [57,58]. The higher the carrier density, the faster the carrier transport is [19]. The carrier densities of H-TiO_2 is higher than that of H-TiO_2@BN, so internal carrier transmission in H-TiO_2 is faster, which also agrees with their photocurrent responses.

3.5. *Proposed mechanism for the photocatalytic H_2 generation on H-TiO_2@BN*

All the above experimental results and analysis indicate that H-TiO_2@BN sample has an excellent photocatalytic activity. Hydrogenated thermal treatment is the key interface engineering process to make H-TiO_2@BN active. As shown in Fig. 9a, TiO_2 nanoparticles supported by BN porous sheets will be crystallized via calcination. However, when TiO_2@BN is annealed at 700 °C in H_2, a significant level of surface disordering is induced with exhibiting a bandgap narrowing as shown in Fig. 4b, which will harvest more visible light photons resulting in more photogenerated electrons. The disordered states induce mid-gap states that were derived from the hybridization of O 2p and Ti 3d orbitals; the optical transition between the mid-gap states and the CB would produce charge transfer from the O 2p orbital to the Ti 3d orbital, similar to the transition from VB to CB in black TiO_2 [18,19]. The mechanism of H-TiO_2@BN for the photocatalytic H_2 production is proposed in Fig. 9b. The Ti-B chemical bonds on the interface between TiO_2 and BN can efficiently facilitate the

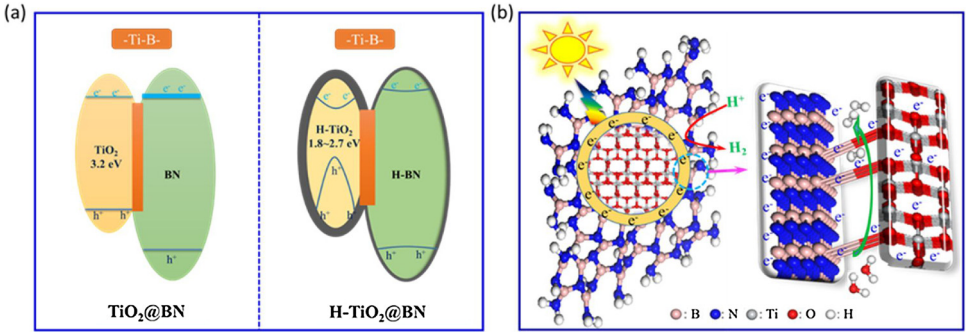

Fig. 9. (a) The band structures of TiO_2@BN and H-TiO_2@BN samples; (b) Proposed mechanism for the photocatalytic H_2 production of H-TiO_2@BN samples.

interfacial electron transfer for electron − hole separation. The photo-generated electrons on TiO_2 should transfer from TiO_2 to BN through the grain boundaries (GB). When a potential barrier is formed at the GB regions, the mobility of electrons could be limited. Thus, the chemical binding of Ti-B could lower the GB potential barrier for efficient charge transfer from TiO_2 to BN [44,46,59]. The Ti-B bonded interface also increases the visible light absorption along with the enhanced charge transfer. In the TiO_2@BN hybrid photocatalysts, they have the similar CB edge position thus the photo-generated electrons in TiO_2 transfer to BN surface without excessive interface recombination or quasi-Fermi level splitting [43,60]. Furthermore, the disordered surface induced by hydrogenated treatment generates many active defect sites for efficient charge generation and separation [61]. More electrons generated and trapped on the disordered surface of H-TiO_2@BN should facilitate the H_2 production reaction. Therefore, the disorder-engineered black H-TiO_2@BN with chemical bonded interfaces harvests the visible light photons more efficiently to generate more electrons and hinders fast recombination by trapping photogenerated electrons at the defect sites, which should make the interfacial electron transfer to protons efficient (as illustrated in Fig. 9b).

4. Conclusion

In summary, H-TiO_2@BN with the Ti-B chemically bonded interface was synthesized using BN nanosheets as the photocatalyst supports. The hybridization with BN and the hydrogenated treatment work synergistically to maximize the H_2 production activity of H-TiO_2@BN, which is comparable to the photocatalytic activity of Pt-TiO_2. In accordance with the highest photocatalytic activity of H-TiO_2@BN, it exhibited the markedly enhanced light absorption, significantly retarded charge pair recombination, facilitated interfacial electron transfer, and lower charge transfer resistance in comparison with TiO_2@BN. In such hybrid photocatalysts, the disorder-engineered black H-TiO_2@BN harvests the visible photons efficiently to generate more electrons and trap more electrons on the defect sites, which should enhance the photocatalytic activity. In particular, the formation of the interfacial Ti-B bonds seems to improve the visible light absorption and the charge transfer capabilities. Such hydrogenated interface engineering for the charge separation and transfer via the formation of the interfacial chemical bonds should provide a new tool for developing efficient photocatalysts.

Acknowledgements

This research was financially supported by the Global Research Laboratory (GRL) Program (No. NRF-2014K1A1A2041044), Basic Science Research Program (NRF-2017R1A2B2008952), and the framework of international cooperation program (NRF-2017K2A9A2A11070417), which were funded by the Korea Government (MSIP) through the National Research Foundation of Korea (NRF).

Appendix A. Supplementary data

Supplementary material related to this article can be found, in the online version, at doi:https://doi.org/10.1016/j.apcatb.2018.06.008.

References

[1] X. Chen, S. Shen, L. Guo, S.S. Mao, Chem. Rev. 110 (2010) 6503–6570.
[2] X. Zou, Y. Zhang, Chem. Soc. Rev. 44 (2015) 5148–5180.
[3] X. Li, J. Yu, M. Jaroniec, Chem. Soc. Rev. 45 (2016) 2603–2636.
[4] Z. He, W. Que, Appl. Mater. Today 3 (2016) 23–56.
[5] G. Zhang, G. Kim, W. Choi, Energy Environ. Sci. 7 (2014) 954–966.
[6] Y. Liao, H. Zhang, Z. Zhong, L. Jia, F. Bai, J. Li, P. Zhong, H. Chen, J. Zhang, ACS App. Mater. Interfaces 5 (2013) 11022–11028.
[7] F. Raziq, L. Sun, Y. Wang, X. Zhang, M. Humayun, S. Ali, L. Bai, Y. Qu, H. Yu, L. Jing, Adv. Energy Mater. 8 (2018) 1701580.
[8] Y. Liao, H. Zhang, W. Que, P. Zhong, F. Bai, Z. Zhong, Q. Wen, W. Chen, ACS Appl. Mater. Interfaces 5 (2013) 6463–6466.
[9] S.J. Moniz, S.A. Shevlin, D.J. Martin, Z.X. Guo, J. Tang, Energy Environ. Sci. 8 (2015) 731–759.
[10] M.V. Dozzi, G.L. Chiarello, M. Pedroni, S. Livraghi, E. Giamello, E. Selli, Appl. Catal. B: Environ. 209 (2017) 417–428.
[11] Z. He, W. Que, J. Chen, X. Yin, Y. He, J. Ren, ACS Appl. Mater. Interfaces 4 (2012) 6816–6826.
[12] Z. He, W. Que, H. Xie, C. Jing, Y. Yuan, S. Peng, J. Am. Ceram. Soc. 95 (2012) 3941–3946.
[13] J.F. de Brito, F. Tavella, C. Genovese, C. Ampelli, M.V.B. Zanoni, G. Centi, S. Perathoner, Appl. Catal. B: Environ. 224 (2018) 136–145.
[14] D. Pan, Z. Han, Y. Miao, D. Zhang, G. Li, Appl. Catal. B: Environ. 229 (2018) 130–138.
[15] H. Yu, W. Liu, X. Wang, F. Wang, Appl. Catal. B: Environ. 225 (2018) 415–423.
[16] X. Chen, L. Liu, Y.Y. Peter, S.S. Mao, Science 331 (2011) 746–750.
[17] X. Liu, G. Zhu, X. Wang, X. Yuan, T. Lin, F. Huang, Adv. Energy. Mater. 6 (2016) 1600452.
[18] A. Naldoni, M. Allieta, S. Santangelo, M. Marelli, F. Fabbri, S. Cappelli, C.L. Bianchi, R. Psaro, V. Dal Santo, J. Am. Chem. Soc. 134 (2012) 7600–7603.
[19] Z. Wang, C. Yang, T. Lin, H. Yin, P. Chen, D. Wan, F. Xu, F. Huang, J. Lin, X. Xie, Energy Environ. Sci. 6 (2013) 3007–3014.
[20] J. Dong, J. Han, Y. Liu, A. Nakajima, S. Matsushita, S. Wei, W. Gao, ACS Appl. Mater. Interfaces 6 (2014) 1385–1388.
[21] H. Cui, W. Zhao, C. Yang, H. Yin, T. Lin, Y. Shan, Y. Xie, H. Gu, F. Huang, J. Mater. Chem. A 2 (2014) 8612–8616.
[22] X. Chen, L. Liu, F. Huang, Chem. Soc. Rev. 44 (2015) 1861–1885.
[23] N. Liu, C. Schneider, D. Freitag, M. Hartmann, U. Venkatesan, J. Müller, E. Spiecker, P. Schmuki, Nano Lett. 14 (2014) 3309–3313.
[24] L. Shen, Z. Xing, J. Zou, Z. Li, X. Wu, Y. Zhang, Q. Zhu, S. Yang, W. Zhou, Sci. Rep. 7 (2017) 41978.
[25] Y. Yu, H. Chen, Y. Liu, V. Craig, L.H. Li, Y. Chen, Adv. Mater. Interfaces 1 (2014) 1300002.
[26] A. Nag, K. Raidongia, K.P. Hembram, R. Datta, U.V. Waghmare, C. Rao, ACS Nano 4 (2010) 1539–1544.
[27] C. Zhang, S. Zhao, C. Jin, A.L. Koh, Y. Zhou, W. Xu, Q. Li, Q. Xiong, H. Peng, Z. Liu, Nat. Commun. 6 (2015) 6519.
[28] J. Grant, C. Carrero, F. Goeltl, J. Venegas, P. Mueller, S. Burt, S. Specht, W. McDermott, A. Chieregato, I. Hermans, Science 354 (2016) 1570–1573.
[29] C. Huang, C. Chen, M. Zhang, L. Lin, X. Ye, S. Lin, M. Antonietti, X. Wang, Nat. Commun. 6 (2015) 7698.
[30] W. Lei, D. Portehault, D. Liu, S. Qin, Y. Chen, Nat. Commun. 4 (2013) 1777.
[31] J. Di, J. Xia, M. Ji, B. Wang, S. Yin, Q. Zhang, Z. Chen, H. Li, Appl. Catal. B: Environ. 183 (2016) 254–262.
[32] Z. He, C. Kim, L.H. Lin, T.H. Jeon, S. Lin, X.C. Wang, W. Choi, Nano Energy 42 (2017) 58–68.
[33] H. Si, G. Lian, J. Wang, L. Li, Q. Wang, D. Cui, C.-P. Wong, ACS Appl. Mater. Interfaces 8 (2016) 1578–1582.

[34] S. Meng, X. Ye, X. Ning, M. Xie, X. Fu, S. Chen, Appl. Catal. B: Environ. 182 (2016) 356–368.
[35] M. Wang, M. Li, L. Xu, L. Wang, Z. Ju, G. Li, Y. Qian, Catal. Sci. Technol. 1 (2011) 1159–1165.
[36] R. Zhang, J. Wang, P. Han, J. Alloys Compd. 637 (2015) 483–488.
[37] C. Gautam, C.S. Tiwary, S. Jose, G. Bruneto, S. Ozden, S. Vinod, P. Raghavan, S. Biradar, D.S. Galvao, P.M. Ajayan, ACS Nano 9 (2015) 12088–12095.
[38] A. Kudo, Y. Miseki, Chem. Soc. Rev. 38 (2009) 253–278.
[39] J. Liu, Q. Jia, J. Long, X. Wang, Z. Gao, Q. Gu, Appl. Catal. B: Environ. 222 (2018) 35–43.
[40] S. Bai, L. Wang, Z. Li, Y. Xiong, Adv. Sci. 4 (2017) 1600216.
[41] X. Wang, S. Blechert, M. Antonietti, ACS Catal. 2 (2012) 1596–1606.
[42] G. Zhou, M.F. Wu, Q.J. Xing, F. Li, H. Liu, X.B. Luo, J.P. Zou, J.M. Luo, A.Q. Zhang, Appl, Catal. B: Environ. 220 (2018) 607–614.
[43] Y. Yang, P. Gao, Y. Wang, L. Sha, X. Ren, J. Zhang, Y. Chen, T. Wu, P. Yang, X. Li, Nano Energy 33 (2017) 29–36.
[44] D. Liu, M. Zhang, W. Xie, L. Sun, Y. Chen, W. Lei, Appl. Catal. B: Environ. 207 (2017) 72–78.
[45] W. Zhao, W. Ma, C. Chen, J. Zhao, Z. Shuai, J. Am. Chem. Soc. 126 (2004) 4782–4783.
[46] Y.Q. Yang, C.H. Sun, L.Z. Wang, Z.B. Liu, G. Liu, X.L. Ma, H.M. Cheng, Adv. Energy Mater. 4 (2014) 1400057.
[47] F. Xiao, Z. Chen, G. Casillas, C. Richardson, H. Li, Z. Huang, Chem. Commun. 52 (2016) 3911–3914.
[48] G. Liu, C. Sun, L. Cheng, Y. Jin, H. Lu, L. Wang, S.C. Smith, G.Q. Lu, H.M. Cheng, J. Phys. Chem. C 113 (2009) 12317–12324.
[49] A. Valdes, Z. Qu, G. Kroes, J. Rossmeisl, J.K. Nørskov, J. Phys. Chem. C 112 (2008) 9872–9879.
[50] Q. Weng, Y. Ide, X. Wang, X. Wang, C. Zhang, X. Jiang, Y. Xue, P. Dai, K. Komaguchi, Y. Bando, D. Golberg, Nano Energy 16 (2015) 19–27.
[51] Y. Yang, G. Liu, J.T.S. Irvine, H.M. Cheng, Adv. Mater. 28 (2016) 5850–5856.
[52] X. Wang, K. Maeda, A. Thomas, K. Takanabe, G. Xin, J.M. Carlsson, K. Domen, M. Antonietti, Nat. Mater. 8 (2009) 76–80.
[53] D.J. Martin, K. Qiu, S.A. Shevlin, A.D. Handoko, X. Chen, Z. Guo, J. Tang, Angew. Chem. Int. Ed. 53 (2014) 9240–9245.
[54] G. Moon, W. Kim, A.D. Bokare, N. Sung, W. Choi, Energy Environ. Sci. 7 (2014) 4023–4028.
[55] Hi. Kim, H. Kim, S. Weon, G. Moon, J.H. Kim, W. Choi, ACS Catal. (2016) 8350–8360.
[56] Y. Choi, H. Kim, G. Moon, S. Jo, W. Choi, ACS Catal. 6 (2016) 821–828.
[57] Z. Feng, X. Cheng, C. Dong, L. Xu, X. Li, Corros. Sci. 52 (2010) 3646–3653.
[58] Z.H. Xue, H. Su, Q.Y. Yu, B. Zhang, H.H. Wang, X.H. Li, J.S. Chen, Adv. Energy Mater. 7 (2017) 1602355.
[59] Q. Huang, S. Tian, D. Zeng, X. Wang, W. Song, Y. Li, W. Xiao, C. Xie, ACS Catal. 3 (2013) 1477–1485.
[60] J.K. Katahara, H.W. Hillhouse, J. Appl. Phys. 116 (2014) 173504.
[61] Q. Ke, C. Guan, X. Zhang, M. Zheng, Y.W. Zhang, Y. Cai, H. Zhang, J. Wang, Adv. Mater. 29 (2017) 1604164.